# A STUDY OF ELECTRONS ARTIFICIALLY INJECTED INTO THE GEOMAGNETIC FIELD IN OCTOBER, 1962*

J. R. BURROWS AND I. B. MCDIARMID
*Division of Pure Physics, National Research Council, Ottawa, Canada*
Received May 25, 1964

ABSTRACT

Particle detectors in the Alouette satellite measured the electrons with energy greater than 3.9 MeV which were trapped in the geomagnetic field as the result of three Russian high-altitude nuclear explosions in October and November, 1962. The early spatial distribution is reported. Temporal variations in the flux have been studied during the following three months. Effects of geomagnetic conditions on the electron precipitation are measured and an estimate is made of the total precipitation at $L \sim 2.95$.

## INTRODUCTION

The injection of electrons, presumed to result from $\beta$ decay of fission fragments, from a series of three Russian high-altitude nuclear explosions in late October and November, 1962, into the region of the magnetic field lying between $L$ of 1.75 and 5.5 earth radii provided a source of energetic electrons, trapped in the earth's field, whose loss rate could be studied as a function of position, time, and geomagnetic conditions. Particle observations from two similar earlier tests have been published. The "Starfish" explosion in July, 1962, was at a lower geomagnetic latitude (Collected papers 1963), and the "Argus" series of three bursts in August, 1958, was at a similar geomagnetic latitude to the present tests (Van Allen, McIlwain, and Ludwig 1959). Of particular interest are problems related to injection processes and the types of loss mechanisms that operate in the magnetosphere. No single experiment can observe all aspects of such widespread phenomena. Therefore, the publication of data for comparison with other spacecraft and ground observations is necessary before a comprehensive picture of the events is available.

This paper will present data from the Alouette satellite particle detectors—first, for the time shortly after injection and, secondly, for the long-term decay characteristics of the trapped belt of electrons.

## DETECTORS

The Alouette satellite is in a nearly circular orbit at an altitude of 1025 ± 20 km, an inclination of 80°, and an orbital period of about 105 minutes. The satellite spins stably with a period of about 45 seconds. This study uses data obtained while the satellite was above the horizon of telemetry stations in the South Atlantic, Canada, Alaska, Australia, and England. Counter A, the principal detector used, is an Anton type 302 geiger counter shielded by 1.4 g cm$^{-2}$ of medium-$Z$ material over 2.4 steradians and by a much greater thickness over the remaining solid angle. The 2.4-steradian aperture extends in a "quadrant"

*Issued as N.R.C. No. 8020.

140° along the satellite equator and from the equator to the spin axis. This shielding gives a calculated electron threshold at 2.8 MeV for the counter and 50% transmission at 3.9 MeV. The two geiger counters B and C are of the Anton 223 end-window type. They make directional measurements of lower-energy electrons collimated through a narrow angle (~5°). For high-energy electrons the minimum shielding is 1.4 g $cm^{-2}$ which is similar to counter A, but extends over somewhat smaller solid angles. The detectors' geometric factors appropriate for energetic electrons are summarized in Table I. A complete description of the package instrumentation is given in an earlier publication (McDiarmid *et al.* 1963).

TABLE I

| | Omnidirectional geometric factor, $cm^2$ | Solid angle for minimum shielding of 1.4 g $cm^{-2}$, sterad | Directional geometric factor, $cm^2$ sterad |
|---|---|---|---|
| Counter A | Over 0.53 | 2.4 | |
| Counter B | Over 0.22 | 2.0 | $5.05\times10^{-4}$ |
| Counter C | Over 0.22 | 0.4 | $2.33\times10^{-3}$ |

In general, the counting rate is integrated for 10-second intervals of flight and in the figures the counting-rate variation due to spin of the satellite in the anisotropic flux is smoothed to give the best estimate of omnidirectional flux. Finer time resolution of the data is available from manual scaling of paper charts, and this is used to get 2-second resolution of data when large flux variations occur during a short time.

A one-component magnetometer provides information about the satellite axis orientation. This is used to obtain the direction of the collimator apertures of the two-directional detectors.

## COORDINATE SYSTEM AND REGION OF MEASUREMENT

Since the satellite is in a nearly circular orbit at 1025 km altitude and 80° inclination, it may seem most reasonable to use the $R$–$\lambda$ coordinate system in mapping the particle fluxes, since $R$, the radial distance from the center of the earth's magnetic dipole, remains nearly constant during any pass over a single telemetry station, and $\lambda$, the invariant latitude at the satellite altitude, varies nearly linearly with time. Thus, particle fluxes could be presented as functions of one spatial coordinate, $\lambda$. However, for the purposes of comparison with data from other satellites, it is felt that a $B$–$L$ coordinate system similar to that given by McIlwain (1961) is more useful. Briefly, in this magnetic coordinate system, $B$ is the magnetic field strength and $L$ is a parameter which characterizes the shell swept out by a trapped particle as it drifts in longitude. By definition (McDiarmid, Burrows, Budzinski, and Rose 1963), $L = (M/B_0)^{\frac{1}{3}}$, where $B_0$ is the minimum field strength (the equatorial value) on the lines of force constituting the shell and $M$ is the dipole moment of the earth. The position on the shell is defined by $B$, the scalar value of the magnetic field. Values of $B_0$ and $B$ are calculated from a spherical harmonic expansion of the earth's

field in which the 48 coefficients are determined from surface measurements of the field. In this system, a locus of $B$ and $L$ which is constant to better than 1% is traced out by the mirror points of a trapped particle as it drifts in longitude around the earth, if the invariants of the particle motion are conserved.

Because of the distortions in the earth's magnetic field, the satellite is able to observe a range of values of $B$ on any given shell $L$, even though the orbit is circular. These regions of measurement are shown in Fig. 1. The longitude of observation is indicated for selected satellite passes which represent the limits of $B$–$L$ space observed by the satellite. Other passes fall within the hatched

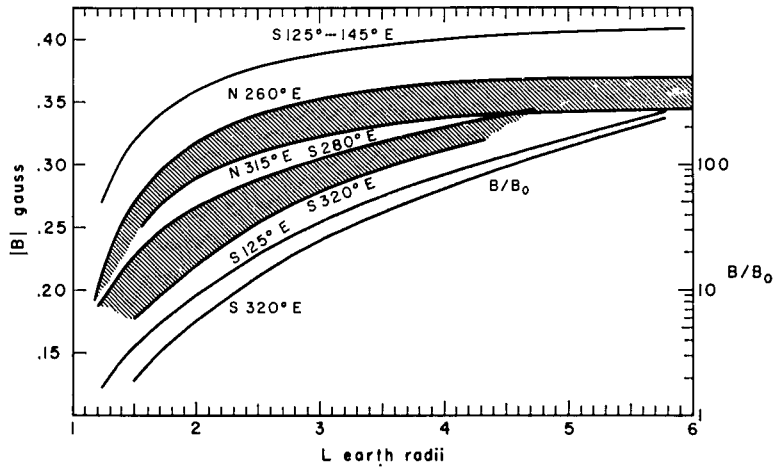


FIG. 1. The regions in $B$–$L$ coordinates and $B/B_0$–$L$ coordinates accessible to the Alouette satellite orbit. Longitudes of passes corresponding to the boundary of each region are given.

region. It can be seen that the lowest portions of the shells are observed over Australia (South 125°–145° E.), intermediate regions are observed over North America, and higher portions of the shell are seen over South America. The bottom hatched region shows the satellite's region of measurement in $B/B_0$ and $L$ coordinates. It can be seen that this region is far from the equator during most of the orbit.

The characteristic motions of trapped particles in the earth's field have been discussed fully by several authors (Hamlin, Karplus, Vik, and Watson 1961; Van Allen 1963). $\tau_2$, the period of oscillation along a field line from mirror point to mirror point, and $\tau_3$, the period of eastward longitudinal drift around the earth, are summarized in Table II for several electron energies of interest in this experiment, on several shells, and for the case of mirror points near 1000 km.

## TRAPPED ELECTRONS SHORTLY AFTER INJECTION

The three nuclear explosions which injected fission-decay electrons into trapped orbits in the earth's field occurred on October 22 and 28 and November 1, i.e., days 295, 301, and 305 of 1962. E.L.F. measurements have placed the times of the first two explosions at 295:03:40:46 ± 3 seconds G.M.T. and

TABLE II

| Energy, MeV | $L$, earth radii | $\tau_2$, seconds | $\tau_3$, minutes |
|---|---|---|---|
| 2.8 | 1.8 | 0.21 | 18.6 |
| 2.8 | 4.0 | 0.46 | 9.3 |
| 3.9 | 1.8 | 0.21 | 14.0 |
| 3.9 | 4.0 | 0.46 | 6.9 |
| 10 | 1.8 | 0.21 | 5.7 |
| 10 | 4.0 | 0.46 | 2.9 |

301:04:41:18 ± 5 seconds G.M.T. (Selzer, private communication, 1964). The effect of the third explosion on the phase of a v.l.f. signal has been observed in eastern Canada at 305:09:13 (Belrose and Ross 1964). This effect is attributed to nearly instantaneous phenomena. The detonations had an equivalent t.n.t. power of several hundred kilotons (Egeland, Lindquist, Riedler, and Petersen 1963). Nothing has been published about the precise altitudes of the explosions.

Fission electrons from the first explosion were first observed by Alouette detectors during pass 313 at 295:04:26. This pass is shown in Fig. 2. The background prior to the explosion is also shown in passes 307 and 312. The intensity scale is based on the solid-angle aperture of 2.4 steradians, although most of the background below $L = 3.5$ is due to cosmic radiation entering over

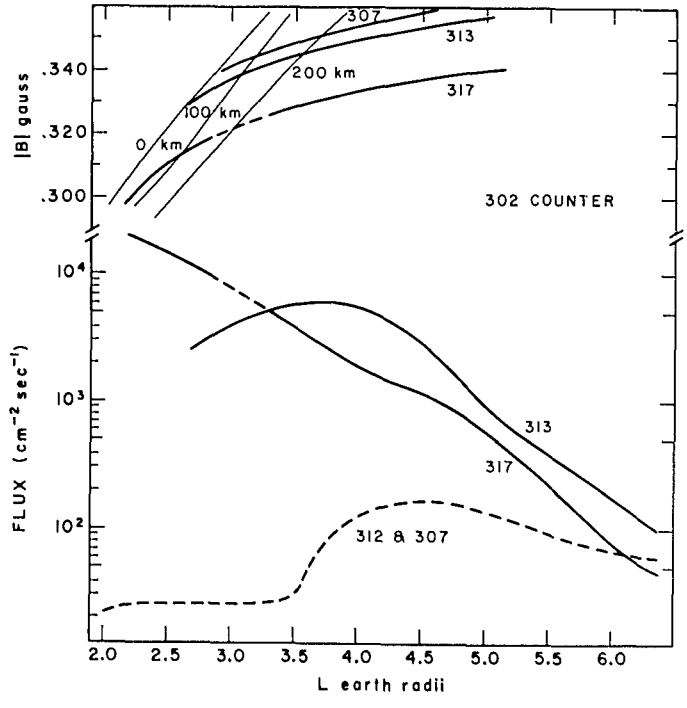


FIG. 2. Omnidirectional electron flux >3.9 MeV vs. $L$ for passes before and after the first explosion. Pass trajectories and loci of minimum mirror-point altitudes are shown in $B$–$L$ coordinates. Pass times: 307 at 294:17:35; 312 at 295:02:45; 313 at 295:04:25; 317 at 295:11:05.

an aperture of at least $2\pi$ steradians. The energetic electrons of the natural outer belt extend from $L = 3.5$ to 6.5. In pass 313, the explosion injected electrons to beyond $L = 6.0$ earth radii. The decrease in intensity for $L < 3.5$ is not a property of the injection since a later pass, 317, shows a continuous increase to the end of the pass at $L = 2.2$. The decrease results from small-angle scattering and loss of the particles as they drift through the South Atlantic magnetic anomaly, where the mirror points penetrate deep into the atmosphere (Welch and Whitaker 1959). The $B$–$L$ trajectories of the three passes are plotted at the top of Fig. 2. In the South Atlantic anomaly area, the mirror points reach their minimum altitudes, and contours in $B$–$L$ space of three minimum altitudes, at 0, 100, and 200 km, are shown. These contours were obtained from graphs published by the United States Defense Atomic Support Agency (Dudziak, Kleinecke, and Kostigen 1963). Since injection was about 50 minutes earlier, the intensity attenuation observed in pass 313 is the result of at least four passages through the anomaly. Most of the electrons observed at $L < 3.0$ have been scattered down the lines of force in the five minutes after they were last at the longitude of the anomaly.

Figure 3 shows the situation before and after the second explosion. Passes 391 and 393, which occurred before the second explosion, show the electron flux remaining from the first explosion. Passes 391 and 395 have very similar $B$–$L$ paths. It can be seen that the second injection was more restricted spatially than the first, no new electrons being observed beyond $L = 3.0$. The

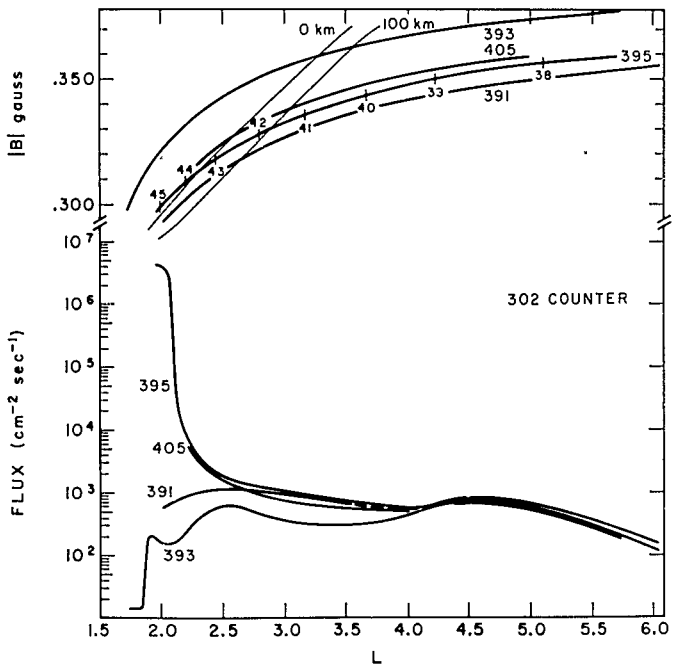


FIG. 3. Omnidirectional electron flux >3.9 MeV vs. $L$ for passes before and after the second explosion. Minute markers on pass 395. Pass times: 391 at 300:21:40; 393 at 301:01:15; 395 at 301:04:45; 405 at 301:22:20.

intense flux at $L = 2.0$ of pass 395 occurs in a region where the mirror points of particles mirroring at the satellite altitude over North America go to an altitude below the earth's surface in the anomaly region. This, therefore, argues that the electrons are being observed during their first eastward drift before suffering scattering and loss by the atmosphere at the anomaly. Pass 395 proceeded from north to south along longitude 200° E. and the minute marks are indicated on the $B$–$L$ trajectory in Fig. 3. The electron flux scale is calculated on the assumption that directly penetrating electrons are being observed with 100% efficiency. Since the drift time from the probable region of the explosion is about four minutes for 3.9-MeV electrons, it is assumed that the electron injection on the field lines occurred immediately after the burst at 301 : 04 : 41 : 18. Thus, the electrons observed during pass 395 have a range of energy which varies from 10 MeV at $L = 2.7$ to 4 MeV at $L = 2.0$. The constant flux observed at the end of the pass ($L \sim 2$) is probably due to the decreasing efficiency of the counter for the lower-energy electrons which are arriving at that time. Although pass 395 cannot be assumed to be the final latitude distribution of electrons above 3.9 MeV, the fact that pass 405, 18 hours after the explosion, shows a similar latitude dependence confirms the observation that very few such electrons were injected beyond $L = 3.0$ by the second explosion.

The third explosion was first observed at 305 : 09 : 19 and longitude 138° E. This pass and the passes of the two preceding days and the following day are shown in Fig. 4. Passes 425 and 439 show some trapped electrons on shells with $L > 1.9$ left from the first and second explosions. Since the $B$–$L$ path of the particle mirror points passes well below the earth's surface when they have drifted eastward into the anomaly, these electrons must have scattered down

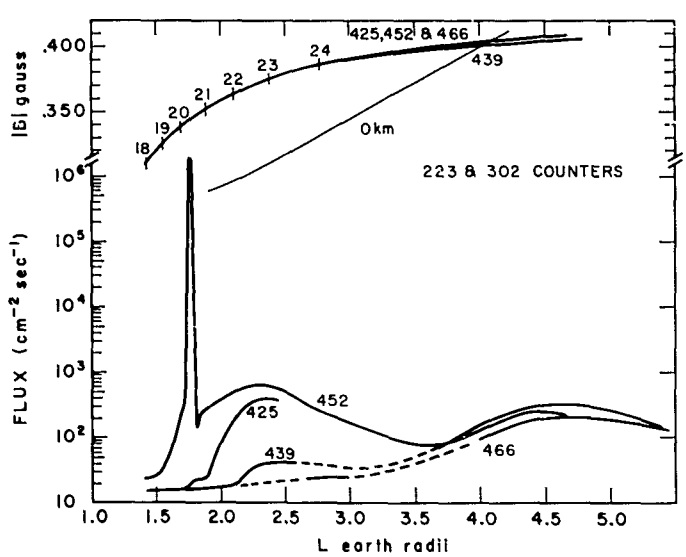


FIG. 4. Omnidirectional electron flux >3.9 MeV vs. $L$ for passes 425, 439, and 466 before and after the third explosion. In pass 452, multiply flux scale by $10^4$ for 1-MeV electrons detected via bremsstrahlung. Minute markers on pass 452. Pass times: 425 at 303:09:50; 439 at 304:10:30; 452 at 305:09:20; 466 at 306:10:00.

the line of force during the five minutes after they last passed through the longitude of the anomaly, i.e., the anomaly centered at 345° E. and observation made at 138° E. The electron distribution seen in pass 452 at $L < 1.9$ is certainly due to new electrons injected by the third explosion. Twenty-four hours later, in pass 466, the intensity has returned to preexplosion levels. The very high intensity in pass 452, centered on $L = 1.76$ and down to 1% of peak intensity at $L = 1.74$ and $L = 1.79$, occurred at 305:09:20:24. Since the explosion is believed to have occurred at 305:09:13, the particles observed by the satellite at $L = 1.76$ have drifted eastward about 70° in 7.5 minutes and from this an energy of 1.0 MeV can be deduced.

An electron with energy above the counter threshold (i.e. >2.8 MeV) requires only 3.6 minutes to drift eastward from the explosion to the point of observation, and unless the injection of these particles is delayed nearly four minutes, they will be well to the east of the satellite longitude at the time of observation. Since so long a delay between the explosion and the injection seems unlikely, it is most probable that the counting rate of all three counters is due to bremsstrahlung from 1-MeV electrons. Some additional information is available from counters B and C. About half of the counting rate in counter C appears to be due to electrons of energy greater than 250 keV entering through the collimator opening. The evidence is as follows.

The corrected counting rate of detector C is about one half of the rate in detector B, whereas a ratio of one fifth is normal for directly penetrating electrons (Table I). It is difficult to calculate the effect of the somewhat irregular shielding around the two counters on the efficiency of the bremsstrahlung conversion process. However, over the minimum shielding regions of the two counters (2.0 steradians and 0.4 steradian respectively) the shielding is similar, and thus the excess rate observed in counter C is thought to be significant. This rate corresponds to a directional flux of electrons with energies greater than 250 keV of $2 \times 10^6$ electrons $cm^{-2}$ $sec^{-1}$ $sterad^{-1}$ in a 50-km-wide region of the maximum intensity. Since the detector was looking up the field line at a pitch angle of 27°, this flux represents electrons with energies greater than 250 keV being precipitated into the atmosphere along the field line of observation.

The intensity scale in Fig. 4 is calculated for energetic electrons penetrating the shielding material, assuming 100% counting efficiency. However, if the electrons in the peak (pass 452) have energies around 1 MeV, as suggested above, then these particles are detected by the bremsstrahlung they produce and, further, if the efficiency of detection by this process is of the order of $10^{-4}$, then the peak omnidirectional flux of 1-MeV electrons 7 minutes after the explosion is $2 \times 10^{10}$ $cm^{-2}$ $sec^{-1}$, which is several thousand times the directly detected intensity of precipitated electrons of similar energy given above. This difference between the trapped and precipitating electron intensities, based on order-of-magnitude estimates, is probably not surprising, since the electrons have already executed about 2000 oscillations between mirror points before reaching the longitude of observation, so that a quasi-stabilized pitch angle distribution will be observed.

Observation of omnidirectional intensities with counters A and B is also possible at points somewhat nearer the equator on the same shells. These data fall in the cross-hatched area of Fig. 1, which corresponds to passes over South America. Passes about 5 hours after the first and second explosions and about 40 minutes after the third explosion are shown in Figs. 5, 6, and 7, along with background measurements prior to each explosion. It can be seen that in all three cases the lower-latitude boundary of the flux is very abrupt. For the first and second explosions the intensity increases by a factor of about seventy within a distance of 70 km ($\Delta L \sim 0.02$). After the third explosion, the low-

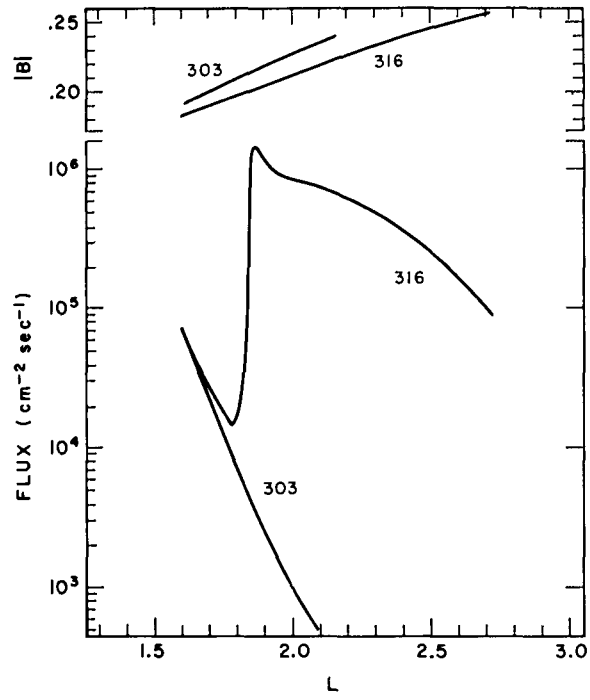


FIG. 5. Omnidirectional electron flux >3.9 MeV vs. $L$ for first explosion. Pass times: 303 at 294:10:00; 316 at 295:08:50.

latitude boundary of the flux increases by a factor of 200 within 90 km ($\Delta L \sim 0.024$). The maximum intensity of the three distributions occurred at $L = 1.88, 1.81(5)$, and 1.77 respectively. The sharp peak of the distribution from the third explosion is shown in Fig. 7. Pass 439 on the previous day at 304:09:13 shows the flux due to particles from the second and first explosions and pass 453 at 305:09:50 shows the added flux from the third explosion. This distribution is almost as narrow as that observed at a larger field strength on the same shell immediately after the explosion (Fig. 4). In contrast, the distribution resulting from the first and second explosions falls off much more slowly with increasing $L$. Figure 5 shows the background prior to the first explosion (pass 303 at 294:10:00) and after the explosion at 295:08:55 (pass 316). Figure 6 shows the flux remaining from the first explosion (pass 391 at 300:22:10) and the contribution of electrons with energy greater than 3.9 MeV from the second

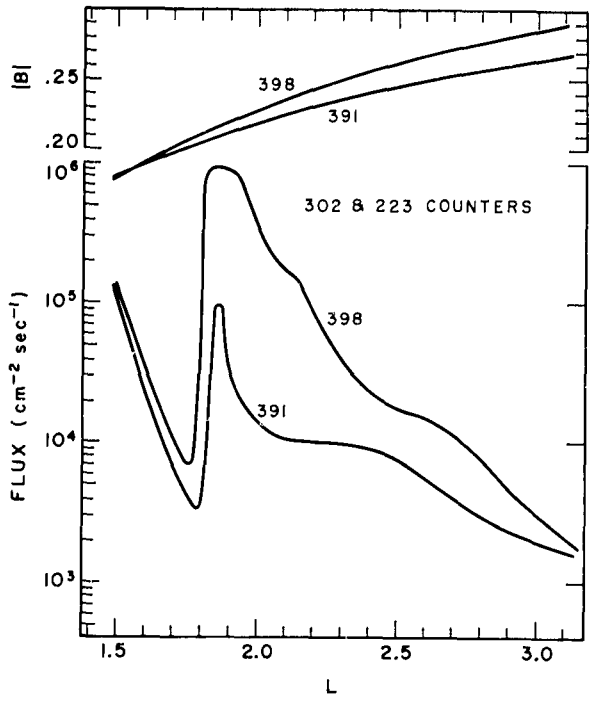


FIG. 6. Omnidirectional electron flux >3.9 MeV vs. $L$ for second explosion. Pass times: 391 at 300:22:10; 398 at 301:09:05.

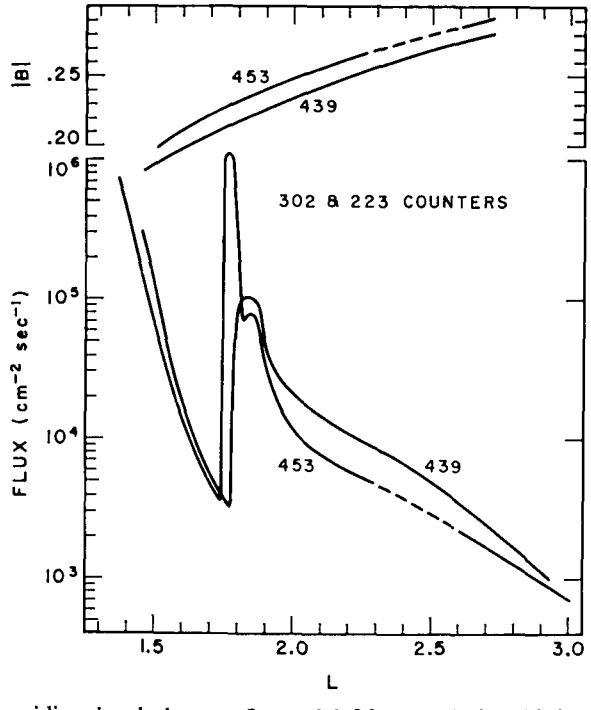


FIG. 7. Omnidirectional electron flux >3.9 MeV vs. $L$ for third explosion. Pass times: 439 at 304:09:10; 453 at 305:09:50.

explosion (pass 398 at 301:09:07). In comparing passes to see the contribution due to newly injected particles, the slightly different trajectories of the passes must be borne in mind. The effect of these differences is seen in the different flux measurements in the region $1.5 < L < 1.7$, which was unaffected by the explosions.

The double peaks centered on $L = 1.83$ and $L = 2.1$ which were observed by Katz, Smart, Paolini, Giacconi, and Talbot (1963) for the burst on October 28 were not observed in these data. Isointensity contours presented by these authors indicate that the Alouette orbit is below the altitude where the double peaks developed.

## DISCUSSION

It would be interesting to be able to relate the spatial distributions of the $\beta$-decay electrons to significant parameters of the explosions such as their altitude and size, if such information becomes available. One must explain the sharp low-latitude boundary which is present in all three distributions, although the higher-latitude distributions vary greatly. The higher-latitude distribution may be a function of explosion altitude with the more limited distributions occurring for lower altitudes as a result of the more dense atmosphere and stronger magnetic field. Under these conditions, preferential funneling along the field line at the explosion site may occur. However, it should be noted that the 90–150 km width of belts from the Argus explosions is similar to the 110-km width of the Russian belt of November 1, 1962, although the Argus explosions all had a high nominal altitude (480 km) and a yield of only 1 to 2 kilotons. The peak flux above 3 MeV from the November 1, 1962, explosion was about ten times greater than that from the Argus shots at similar times after the respective explosions. Thus, the November 1, 1962, explosion was probably larger, say in the submegaton range, but at a lower altitude. Then the tendency of a larger explosion to disperse the $\beta$-decay electrons to higher latitudes might be balanced by the stronger restraints of atmosphere and magnetic field.

## INTENSITY GRADIENT ON A SHELL

In order to obtain an estimate of the spatial distribution of particle intensities along a shell, the passes over South America between the first and second explosion were plotted in Fig. 8. The passes were grouped in 12-hour intervals for six days after the first explosion (groups 0 to 11). The intensity on the $L = 2.0$ shell was determined for detectors A, B, and C. A correction was applied to measured intensities $I_M$ in order to standardize them to a uniform time of two hours after the explosion. The form of the correction used was based on the measured intensity decay shown in Fig. 9. This was

$$\log I_{2\,\mathrm{hr}} = \log I_M + 1.35 \log T/2, \tag{1}$$

where $T$ was the number of hours after the explosion of each measurement. The scatter in the points does not seem to have any systematic change with time during the 6-day interval which adds support to the assumed time decay. The scatter is probably mostly due to the limited solid-angle aperture of the

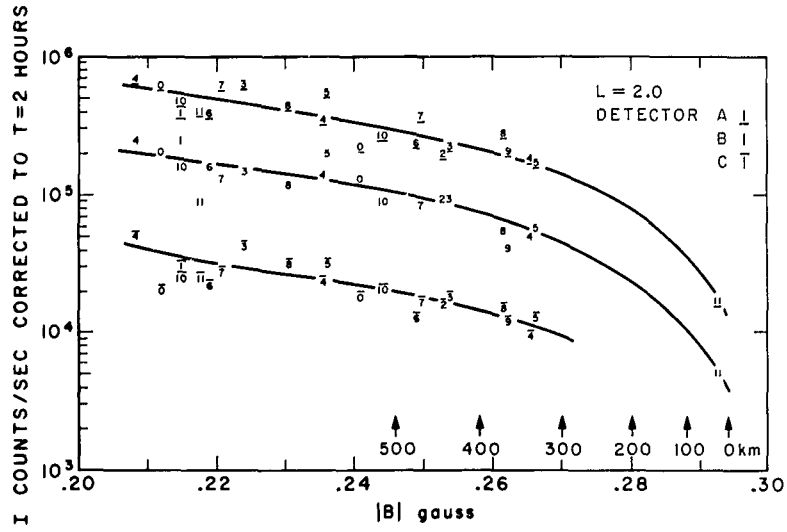


FIG. 8. Counting rate vs. field strength on shell $L = 2.0$ for detectors A, B, and C. Rates corrected to a standard time two hours after the first explosion. Minimum mirroring altitude of some $B$–$L$ loci is indicated.

detectors, which are measuring a particle flux which is anisotropic, having a maximum at right angles to the field line. In all passes, a spin effect was present because of this anisotropic flux, sometimes giving a change of up to a factor of 2 in intensity during the 45-second spin period. Average intensities were taken from smoothed curves. Data from all three of the detectors are plotted to allow an experimental comparison of solid-angle factors. The minimum altitude at which the particles mirror in the magnetic anomaly region is indicated along the bottom, and a sharp decrease in intensity is seen to occur somewhere below 300 km. This, of course, corresponds to increasingly greater loss by atmospheric scattering.

## PARTICLE LOSS RATES

Figure 9 shows the change of intensity of trapped electrons with time. Counter A, which has 50% transmission for 3.9-MeV electrons, was used. The counting rate is plotted against pass number after the first explosion, using logarithmic scales for both axes. The day of the year, from October 22, 1962, to January 25, 1963, is indicated at the top. First-order corrections were made to the counting rate to allow for the different trajectories of the individual passes, using the known change of intensity along a shell as shown in Fig. 8. The counting rate is averaged over an interval $\Delta L = 0.1$ in each case and the data, which have a range of $B$, are corrected to a standard $B$ by applying a first-order correction of the form $\Delta \log I/\Delta B$. These quantities are summarized below in Table III for each decay curve, along with the corresponding ratio $B/B_0$ and the slopes, $\eta$, of the various straight-line portions of the decay.

The dotted lines in Fig. 9 indicate the preexplosion background and two arrows indicate the time of the second and third explosions. It can be seen that

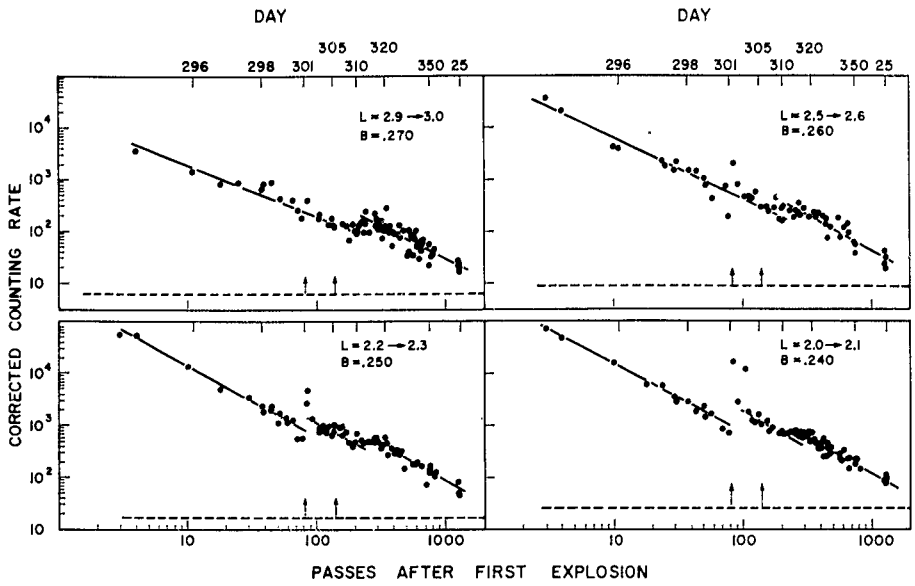


FIG. 9. Counting rate of counter A vs. time after the first explosion on four selected shells. First-order corrections applied to the counting rates standardize them to the indicated field strengths.

TABLE III

| $L$ | $B_{range}$ (gauss) | $B_{stand}$ | $\frac{\log I}{B}$ | $\frac{B}{B_0}$ | $I$ ratio | | $\eta$ | |
|---|---|---|---|---|---|---|---|---|
| | | | | | 1st | 2nd | 1st & 2nd | 3rd |
| 2.0–2.1 | 0.21–0.25 | 0.240 | 11.0 | 6.7 | 2.3 | 1.6 | 1.3(5) | 1.3(5) |
| 2.2–2.3 | 0.23–0.26 | 0.250 | 12.0 | 9 | 1.9 | 1.8 | 1.3(5) | 1.4 |
| 2.5–2.6 | 0.245–0.275 | 0.260 | 12.0 | 14 | | 2.0 | 1.2 | 1.3(5) |
| 2.9–3.0 | 0.27–0.30 | 0.270 | 13.0 | 22 | | 2.3 | 1.0 | 1.3 |

the intensity had not returned to its preexplosion background by the end of January, 1963. Measurable discontinuities in the intensity result from the second explosion up to $L = 2.3$ with an enhancement for only a few passes at $L = 2.55$. The ratios of the intensities at this discontinuity are also listed in Table III. A second "break" in the decay curves is indicated between days 310 and 315. It has the appearance of a uniform intensity for several days at lower $L$ (up to $L = 2.3$) and a positive intensity enhancement at $L = 2.95$. This is not associated with the third explosion, which, as indicated above, occurred on day 305 and injected negligible numbers of 3.9-MeV electrons beyond $L = 1.9$. The intensity ratios of the straight-line sections drawn before and after this second "break" are listed in Table III. The effect is larger at higher $L$. This "break" in the curve does not have any obvious correlation with geomagnetic indices, and at present the authors have no satisfactory explanation of it.

The slopes of the straight lines drawn in Fig. 9 which give the exponent, $\eta$, in the equation $I = I_0 T^{-\eta}$ are also listed in Table III. This exponent is nearly a constant for all latitudes after the second "break", but prior to that time, the

flux decay is a function of $L$. The fitting of the flux decay by a power law is suggested by the theory of Welch and Whitaker (1959). This theory treats the effect of atmospheric small-angle scattering (which occurs principally near the mirror points) on the mirror-point density of trapped electrons, $\omega(h, t)$, considering both particles lost to lower altitudes and those gained from higher altitudes. A mirror-point density, which is a function of the height of the minimum mirror altitude $h$ and of time $t$, is found with the form

$$\omega(h, t) = \omega(h, 0) \frac{\tau}{\tau + t}, \tag{2}$$

where $\tau$ is a characteristic time of less than one day, for the altitudes of interest here. This predicted exponent of $-1.0$ for the decay rate at time greater than one day is smaller than the observed exponents at $L = 2.05$, 2.25, and 2.55 for the early decay and is smaller than all decays observed at later times.

It should be noted that the scatter in the data becomes larger with increasing $L$. This may be due to impulsive geomagnetic loss altering the equilibrium distribution resulting from atmospheric scattering. Evidence of this is presented below.

Figure 10 shows the effect of particle loss due to passage through the anomaly, using two passes which are as near as possible in $B$–$L$ trajectory and universal time and placed on either side of the anomaly. Pass 409 was at 190° E. longitude

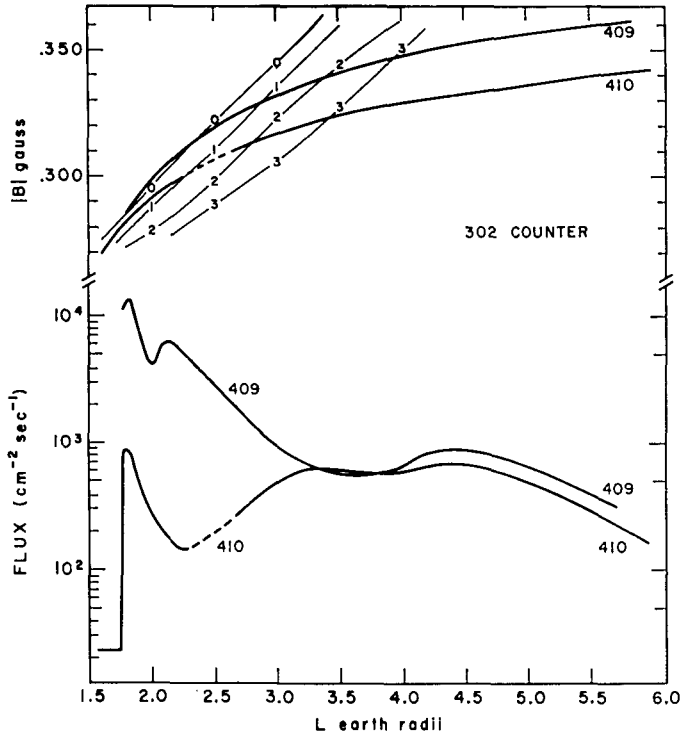


FIG. 10. Omnidirectional electron flux >3.9 MeV vs. $L$ for two consecutive passes on either side of the magnetic anomaly; showing particle loss into the atmosphere.
Pass 409 at 302:05:20. Long. 190° E. Pass 410 at 302:06:40. Long. 15° E.

and pass 410 was at 15° E. longitude about 80 minutes later (six drift periods). The trajectories show that pass 410 occurs higher on the shells (equivalent to about a 100-km difference in the altitude of the minimum mirror point), so that in the absence of the anomaly one might expect to measure a higher flux than in pass 409. However, because pass 410 is observing particle flux immediately after passage through the anomaly, attenuation by a factor of 50 has occurred at $L = 2.2$ and attenuation still occurs out to $L = 3.3$. The $B$–$L$ trajectories indicate that at $L = 3.3$ there is a minimum mirroring altitude of about 250 km in the anomaly. The data shown in Fig. 11 for the range of $L = 2.8$–$3.1$ is, in all cases, taken for field strength greater than 0.330 gauss at $L = 2.90$. Thus the passes, which are recorded over North America, are observing electrons which are lost by atmospheric scattering a few minutes later in the South Atlantic anomaly. Each point corresponds to the average counting rate of counter A for a pass in the interval $2.80 < L < 3.10$. The

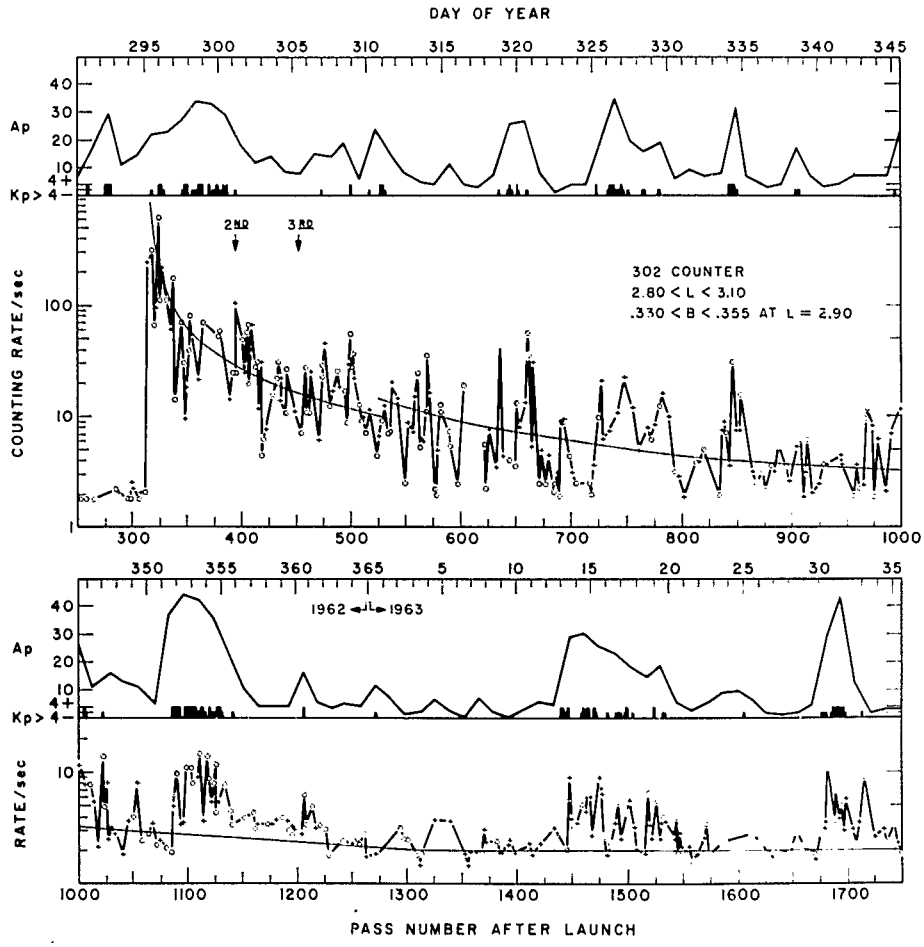


FIG. 11. Counting rate and daily planetary magnetic index $A_p$ vs. time on shell $L = 2.95$ for field strengths of 0.330–0.355 gauss.

passes are divided into two groups, the passes over College, Alaska, marked by crosses and the passes over central Canada (Ottawa and Prince Albert stations) marked by open circles. The College passes have $0.330 < B < 0.340$ and the central Canada passes have $0.340 < B < 0.355$ and are about 75° farther east. In general, there is no systematic difference in counting rate between the two groups. The times of the second and third explosion are indicated by arrows.

The smooth curve, which has a break at pass 525, satisfies the equation $I = I_0\tau^{-\eta}$ with appropriate values of $\eta$. It corresponds to the average decay rate observed in Fig. 9 for this $L$ interval. The curves were positioned to give median lines from pass 313 to 525 and from pass 525 to 1075. After pass 1300 the line is horizontal. It corresponds to the average counting rate in the 10 days before the first explosion, during which time the average $A_p$ index was 17. The break in the median curve at pass 525 corresponds to only a 45% enhancement in counting rate compared to 130% observed higher on the $L$ shell in Fig. 9. Because of the large fluctuations of intensity observed in Fig. 11, the median curves have only limited significance, and the existence, location, and magnitude of a break could not be inferred from the data in Fig. 11 alone. The main features apparent in Fig. 11 are the much larger scatter in the data compared with Fig. 9 and the correlation of intensity increases with times of high geomagnetic indices. The daily planetary amplitude $A_p$ is plotted directly above the particle counting rate and occasions are also indicated when the planetary three-hour index, $K_p$, is greater than 4− and 4+. During the first 10 days after the first explosion, the generally high magnetic activity and the high average particle loss rate make correlation difficult. Later, on days 307, 309, 319–321, 326–329, 334, 345, 351–355, 13–19, and 30–33 significant increases occur during disturbed conditions. The increase on day 343 corresponds to a single three-hourly $K_p = 4^-$ during several quiet days. Enhanced counting rates during days 313, 314, 316, and 322 are not correlated with any disturbed conditions on the $K_p$ or $A_p$ scale.

Fewer passes are available at $L = 2.5$ for a plot of the type presented in Fig. 11. Instead, in Fig. 12 the intensity excess above the average is plotted

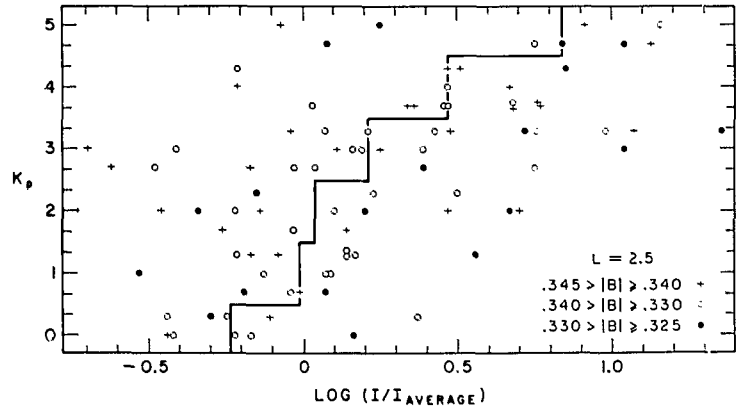


FIG. 12. The planetary 3-hour geomagnetic index $K_p$ vs. log(measured rate of counter A/median rate from Fig. 9) at $L = 2.5$ for three ranges of field strength.

against $K_p$. Counter A is used. Each point represents a pass with the intensity, $I$, averaged for $2.4 < L < 2.6$ divided by $I_{average}$ taken from the decay curve in Fig. 9. An arbitrary addition of 1.5 has been made to the horizontal scale, since the intensity is about a factor of 30 lower around $B = 0.340$ than at $B = 0.260$. The three-hourly value of $K_p$ used corresponds to the time of observation, unless this time falls within the first half-hour of the three-hour interval. In this case the preceding $K_p$ value is used. All passes for nearly two months after the first explosion (pass 324 to 1140) are included. Here again the particles observed are entirely lost by atmospheric scattering in the anomaly, so that the intensity observed at this altitude represents electrons scattered down the shell during the 10 minutes after they last passed through the anomaly. There is no systematic grouping of the points as a function of field intensity at the point of observation. In spite of the large scatter in the points, however, there is a systematic trend in the points which is indicated by the median line calculated for each value of $K_p$. A small enhancement in the precipitated flux of electrons of $E > 3.9$ MeV is seen to occur even during weak magnetic disturbance, and a factor of 10 enhancement occurs for $K_p = 5$, which was the highest $K_p$ coincident with a pass during the two-month interval.

Specific examples, not shown in the diagrams, of intensity increases of more than a factor of 15 which extend into $L \sim 1.9$ are found in a few passes (e.g., day 319:19, $K_p = 4+$; 320:20, $K_p = 3+$; 352:22 and 353:03 $K_p = 5$). They are associated with times of strong disturbance, but do not necessarily occur at times of maximum $K_p$. Also, after periods of prolonged disturbance, precipitation does not necessarily continue with an enhanced intensity and the intensity is sometimes not enhanced at low latitudes until some time after $K_p$ has reached a maximum (e.g., 6 hours on day 319, 18 hours on day 320). This behavior is not surprising since the $K_p$ index is probably only indirectly related to the specific geomagnetic mechanism which results in lowered mirror points and eventual loss of energetic particles at these midlatitudes. The large scatter in the points at $L = 2.5$ in Fig. 12 when $K_p$ is used as the ordinate is, therefore, not unexpected.

To summarize the observations represented by Figs. 9, 11, and 12, we may say that two regions of trapping are being observed. The one, shown in Fig. 9, is a relatively stable region near the lower edge of the trapped-particle reservoir. The electron population is presumably being lost to points lower on the shell and replenished from points higher on the shell, and the overall loss rate is somewhat faster than that theoretically predicted for atmospheric scattering alone. The best fit to the data after the second explosion requires two straight-line sections with a "break" or pause in the flux decay occurring around day 310 to 315. This "break" has no obvious connection with geomagnetic activity but must arise either from a faster redistribution of particles trapped higher on the shells or from an acceleration of particles, already mirroring at the satellite altitude, which brings them above the counter threshold. In the other region quasi-trapped electrons are observed. In Fig. 11 two components can be observed, a steady decay component, resulting from atmospheric scattering, and a large fluctuating component which has a positive correlation with geomagnetic

activity. The fluctuating component tends to predominate at later times. Effects of enhanced precipitation due to geomagnetic activity are observed on shells as low as $L = 1.9$, this being the limit for which sufficient data are available.

## CALCULATED TOTAL PARTICLE LOSS AT $L = 2.9$

It is possible to calculate the total number of particles lost after the explosion from the region $L = 2.8$–$3.1$ based on the following four points:

1. The shape of the median decay curve from Fig. 11.
2. The idea that all of the electrons observed over North America which mirror at $B > 0.330$ gauss are lost in the South Atlantic anomaly. This point is supported by Fig. 10.
3. An insignificant proportion of electrons is lost due to atmospheric scattering at other longitudes. This may be only a lower limit during periods of magnetic disturbance when particles are being pushed down the lines of force at a faster rate.
4. The background due to naturally generated energetic electrons is negligible. Measurements in Fig. 11 prior to the explosion show this to be the case.

The number of particles, $N$, lost over the anomaly per second per centimeter of latitude is

$$N = nv, \tag{3}$$

where $n$ is the number of electrons in a tube of force of 1-cm cross section at 1000 km which mirror below 100 km in the anomaly. This corresponds to $B = 0.330$ gauss at $L = 2.9$. $v$ is the longitudinal drift velocity of particles at 1000 km in cm/sec. To calculate $n$, it is necessary to assume a directional intensity distribution, since a measurement of omnidirectional intensity at a single position on a line of force is insufficient to determine uniquely the value of $n$. Assume that $J$, the omnidirectional flux measurement at 1025 km, results from a directional intensity, $j(\alpha)$, which is a maximum at a pitch angle $\alpha = 90°$ and is zero below $\alpha = 60°$. This corresponds to particles mirroring between 1025 km and 100 km. More specifically, let

$$\begin{aligned} j(\alpha) &= -j_0 \sin 3\alpha, \qquad \tfrac{1}{3}\pi < \alpha < \tfrac{1}{2}\pi, \\ j(\alpha) &= 0, \qquad\qquad\quad 0 < \alpha < \tfrac{1}{3}\pi. \end{aligned} \tag{4}$$

By definition

$$J = \int_{\pi/3}^{2\pi/3} j(\alpha)\mathrm{d}\Omega. \tag{5}$$

Therefore

$$J = \frac{3\pi\sqrt{3}}{4} j_0. \tag{6}$$

Now $n$, as defined above, is also the number of particles that cross a plane of unit cross section at 1000 km, perpendicular to the field line during one bounce period, $\tau$:

$$n = \tau \int_{\pi/3}^{\pi/2} j(\alpha) \cos \alpha \, d\Omega. \tag{7}$$

Combining (6) and (7) gives

$$n = 0.092 J\tau. \tag{8}$$

It might be noted that the result in equation (7) is not affected greatly by alternative choices for $j(\alpha)$. A flat distribution:

$$j(\alpha) = j_0, \qquad \tfrac{1}{3}\pi < \alpha < \tfrac{1}{2}\pi,$$
$$= 0, \qquad 0 < \alpha < \tfrac{1}{3}\pi,$$

gives

$$n = 0.125 J\tau.$$

A linear distribution:

$$j(\alpha) = j_0((6\alpha/\pi) - 2), \qquad \tfrac{1}{3}\pi < \alpha < \tfrac{1}{2}\pi,$$
$$= 0, \qquad 0 < \alpha < \tfrac{1}{3}\pi,$$

gives

$$n = 0.085 J\tau.$$

Using formulae for the bounce period and drift period from Lew (1961) at the invariant latitude 51° and 1025-km altitude, $\tau = 0.31$ sec and $v = 5.5 \times 10^6$ cm/sec. Taking the geometric factor of the detector A for 3.9-MeV electrons from Table I,

$$N = 1.8 \times 10^6 R \text{ cm}^{-1} \text{ sec}^{-1}, \tag{9}$$

where $R$ is the observed counting rate. $R$ is obtained from the area under the median decay curve of Fig. 11 for the first 300 passes after the first explosion and the region $2.8 < L < 3.1$ corresponds to $3 \times 10^7$ cm of latitude. A resulting particle loss during the 300 passes (525 hours) immediately after the explosion of $3 \times 10^{21}$ electrons is obtained for $2.8 < L < 3.1$.

## CONCLUSIONS

Some $\beta$-decay electrons with energy greater than 3.9 MeV were trapped in the geomagnetic field as the result of three Russian high-altitude nuclear explosions. All three spatial distributions showed a sharp low-latitude boundary. The high-latitude boundary of the third explosion was sharp, but for the others it was diffuse, extending up to 6.0 earth radii. The trapped electron flux at 1000 km diminished according to a power relation in time with exponent $-1.0$ to $-1.4$. The precipitating electron flux showed intensity variations correlated with magnetic indices at $L = 2.95$ and 2.5 and in specific cases as low as $L = 1.9$. An estimate of total precipitation during the first 525 hours in the region $2.8 < L < 3.1$ gives no less than $3 \times 10^{21}$ electrons with energy above 3.9 MeV.

## ACKNOWLEDGMENTS

We wish to thank the Defence Research Telecommunications Establishment of the Defence Research Board of Canada and the United States National

Aeronautics and Space Administration for the opportunity to carry out these experiments in the Alouette satellite, and the staff of the seven telemetry stations from which data were obtained. We are also grateful to Dr. Margaret D. Wilson, who provided computer programming assistance in the reduction of the data.

## REFERENCES

BELROSE, J. S. and Ross, B. B. Can. J. Phys. To be published.
COLLECTED PAPERS on the artificial radiation belt from the July 9, 1962, nuclear detonation. 1963. J. Geophys. Res. **68**, 605.
DUDZIAK, W. F., KLEINECKE, D. D., and KOSTIGEN, T. J. 1963. Graphic displays of geomagnetic geometry RM 63 TMP-2 DASA 1372.
EGELAND, A., LINDQUIST, R., RIEDLER, W., and PETERSEN, A. 1963. Nature, **198**, 1076.
HAMLIN, D. A., KARPLUS, R., VIK, R. C., and WATSON, K. M. 1961. J. Geophys. Res. **66**, 1.
KATZ, L., SMART, D., PAOLINI, F. R., GIACCONI, R., and TALBOT, R. J. 1963. Measurements on trapped particles injected by nuclear detonations, *presented at* Trapped Radiation Symposium NASA.
LEW, J. S. 1961. J. Geophys. Res. **66**, 2681.
McDIARMID, I. B., BURROWS, J. R., BUDZINSKI, E. E., and ROSE, D. C. 1963. Can. J. Phys. **41**, 1332.
McILWAIN, C. E. 1961. J. Geophys. Res. **66**, 3681.
SELZER, E. 1964. University of Paris. Private communication.
VAN ALLEN, J. A. 1963. Space science (John Wiley and Sons, Inc.), Chap. 7.
VAN ALLEN, J. A., McILWAIN, C. E., and LUDWIG, G. H. 1959. J. Geophys. Res. **64**, 877.
WELCH, J. A. and WHITAKER, W. A. 1959. J. Geophys. Res. **64**, 909.